NeuroImage 210 (2020) 116523

Contents lists available at ScienceDirect

NeuroImage

journal homepage: www.elsevier.com/locate/neuroimage

Correlative x-ray phase-contrast tomography and histology of human brain tissue affected by Alzheimer's disease

Mareike Töpperwien [a], Franziska van der Meer [c], Christine Stadelmann [c], Tim Salditt [a,b,*]

[a] Institute for X-Ray Physics, University of Göttingen, Germany
[b] Cluster of Excellence "Multiscale Bioimaging: from Molecular Machines to Networks of Excitable Cells", University of Göttingen, Germany
[c] Institute for Neuropathology, University Medical Center Göttingen, Germany

ARTICLE INFO

Keywords:
phase-contrast x-ray tomography
Synchrotron-based x-ray imaging
Laboratory-based x-ray imaging
Alzheimer's disease
Correlative imaging

ABSTRACT

Alzheimer's disease (AD) is a neurodegenerative disorder which is characterized by increasing dementia. It is accompanied by the development of extracellular β-amyloid plaques and neurofibrillary tangles in the gray matter of the brain. Histology is the gold standard for the visualization of this pathology, but also has intrinsic shortcomings. Fully three-dimensional analysis and quantitative metrics of alterations in the tissue structure require a complementary approach. In this work we use x-ray phase-contrast tomography to obtain three-dimensional reconstructions of human hippocampal tissue affected by AD. Due to intrinsic electron density differences, tissue components and structures such as the granule cells of the dentate gyrus, blood vessels, or mineralized plaques can be identified and segmented in large volumes. Based on correlative histology, protein (tau, β-amyloid) and elemental content (iron, calcium) can be attributed to certain morphological features occurring in the entire volume. In the vicinity of senile plaques, an accumulation of microglia in combination with a loss of neuronal cells can be observed.

1. Introduction

Alzheimer's disease (AD) is an age-related neurodegenerative disease which leads to memory loss and a decrease in cognitive functions. The pathology is characterized by an intra-neuronal aggregation of neurofibrillary tangles (NFT) due to an abnormal hyperphosphorylation of Tau protein, formation of extracellular plaques from β-amyloid protein and massive neuronal death. These hallmarks occur in specific areas of the brain of which the hippocampus is one of the earliest to be affected (Mu and Gage, 2011). The gold standard for the visualization of AD pathology is histology, a destructive imaging technique which uses different staining protocols to image specific features of the sample in a slice-by-slice manner. This leads to impressive results on the individual two-dimensional (2d) sections (Perl, 2010), while the three-dimensional (3d) anatomy has to be reproduced by aligning these sections (Ourselin et al., 2001) or developing automatic systems with accurate spatial positioning (Li et al., 2010), resulting in a reconstructed volume with non-isotropic resolution. A direct non-destructive visualization of the 3d structure can be obtained by x-ray phase-contrast tomography which images the sample based on electron density differences, and also provides a fully digitalized representation of the structure. In contrast to classical computed tomography (CT), which relies on the absorption of (hard) x-rays while passing through the sample, phase-contrast tomography exploits the phase shift induced by the sample for contrast formation. As differences in phase shift result in much higher sensitivity for soft tissue structures than absorption contrast, this is a necessary prerequisite to resolve the underlying cytoarchitecture. Several methods exist to make the phase shift visible in the recorded intensity images, e.g., diffraction-enhanced imaging (Chapman et al., 1997), interferometric methods using crystals (Momose et al., 1996), grating-based imaging (Pfeiffer et al., 2008; Bech et al., 2010), speckle-based imaging (Zanette et al., 2014) or free space propagation between the object and the detector (Paganin and Nugent, 1998). These techniques do not yet reach the resolution provided by ptychography (Deng et al., 2018) but have the advantage of large fields of view as they do not require scanning over the sample. In previous studies, full-field phase contrast tomography has been applied to transgenic mouse models for Alzheimer's disease (Noda-Saita et al., 2006; Connor et al., 2009; Pinzer et al., 2012; Astolfo et al., 2016; Massimi et al., 2019), showing considerable contrast for β-amyloid plaques as one of the typical hallmarks associated with this disease. The development of suitable

* Corresponding author. Institute for X-Ray Physics, University of Göttingen, Germany
E-mail address: tsaldit@gwdg.de (T. Salditt).

https://doi.org/10.1016/j.neuroimage.2020.116523
Received 17 May 2019; Received in revised form 1 November 2019; Accepted 5 January 2020
Available online 11 January 2020

mouse models is essential in order to gain insights into the biological basis of the disease or test different therapeutic approaches (Elder et al., 2010). Many mouse models exist which develop the typical plaque pathology, including dystrophic neurites, reactive astrocytes and activated microglia, as well as accompanying cognitive deficits. However, it remains challenging to produce the full spectrum of AD pathologies in these models, especially with regard to NFT-like lesions. Additionally, the temporal appearance of pathology and cognitive decline is different compared to human cases and the genetic mutations used for the models are based on familial AD which only affects a small subset of patients. Due to this lack of truly complete mouse models for Alzheimer's disease it is critical to extend x-ray phase contrast studies to human brain tissue to unravel the underlying structural alterations associated with the disease itself.

In this study, we demonstrate x-ray phase-contrast tomography based on free space propagation on paraffin-embedded hippocampal human tissue affected by Alzheimer's disease, and evaluate its capability to visualize different pathologies, including plaques, depletion of neurons or possible recruitment of microglia to affected sites. We have performed experiments both at a home-built laboratory μCT setup equipped with a liquid-metal jet microfocus source (Hemberg et al., 2003; Bartels et al., 2013; Töpperwien et al., 2018) as well as a high-resolution holo-tomography endstation installed at the PETRAIII storage ring in Hamburg, which was developed by our group. By careful optimization of optical and geometrical parameters as well as reconstruction algorithms, this enables imaging of the 3d cytoarchitecture of paraffin-embedded human brain tissue at (sub-)cellular resolution (Töpperwien et al., 2018). In order to correlate the structures observed via phase-contrast tomography with the underlying AD pathology, we combine these experiments with subsequent histological sectioning using specific staining protocols. Validation of x-ray tomography via comparison with the well known histological assessment was demonstrated earlier, e.g, via a standard H&E stain for imaging of human coronary arteries (Holme et al., 2014; Vågberg et al., 2018), as well as cerebellum (Hieber et al., 2016; Khimchenko et al., 2018). Here we extend this correlative approach to specific labels relevant for AD, enabling a precise evaluation of x-ray contrast for different structural hallmarks of AD. We show that unlike in the previously reported mouse models of Alzheimer's disease, senile plaques in human tissue show a much smaller electron density, unless they are mineralized. This indicates a fundamental structural difference between transgenic mouse models and the actual disease. At the same time, we observe an accumulation of microglia in combination with a loss of neuronal cells in the vicinity of senile plaques.

2. Materials and methods

2.1. Sample preparation

Human brain tissue from an 81 year old patient with Alzheimer's disease was obtained at autopsy. The intact brain was immersion-fixed in 10% neutral buffered formalin for several weeks, dissected, and relevant brain regions (maximum size of each 2.5 × 2.0 × 0.5 cm) were processed using an ExcelsiorTM AS automatic tissue processor (Thermo Fisher Scientific) with a 36-h protocol. A series of graded ethanol baths starting from 50% and progressing to 100% was used to dehydrate the tissue followed by a washing step with xylene to replace ethanol with a substance that is miscible with paraffin. The tissue finally underwent paraffin infiltration at 63° C, and was embedded into paraffin blocks, also commonly denoted as FFPE (formalin-fixed, paraffin-embedded) tissue blocks. Hematoxylin-eosin staining, Bielschowsky silver impregnation and immunohistochemistry for hyperphosphorylated tau and βA4 were performed on hippocampal sections for routine diagnostic purposes. Tau and amyloid pathology were rated according to current diagnostic guidelines (Hyman et al., 2012). The study was approved by the ethics committee of the University Medical Center Göttingen.

For the CT experiments, a 1 mm biopsy punch was taken from the embedded tissue and was subsequently transferred into a Kapton tube glued to a sample holder. In this way, unnecessary absorption and local tomography artifacts by contributions of the sample outside the field of view were avoided. The region of the dentate gyrus was chosen for the location of the punch, as can be seen in Suppl. Fig. S1 on the left, showing a histological section of the hippocampal region after the punch was taken.

2.2. Experimental setups

2.2.1. Laboratory setup

A sketch of the laboratory setup (Bartels et al., 2013; Töpperwien et al., 2017, 2018) is shown in Fig. 1 (a). The x-rays are generated by a liquid-metal jet microfocus source (Excillum, Sweden) which enables a small source spot while providing a high photon flux. The anode material is the metal alloy Galinstan (68% Ga, 22% In, 10% Sn) with a main characteristic energy at the Ga-K_α line at 9.25 keV. The source was operated at an acceleration voltage of 40 keV with an electron power of 57 W. The electron spot size was set to 10×40 μm^2, leading to an approximately circular projected source size of 10 μm (FWHM). In a distance z_{01} the sample is placed on a motorized sample stage, allowing for the positioning of the rotation axis in the center of the detector as well as the region of interest within the sample in the field of view. A scintillator-based lens-coupled CCD detector with a pixel size of 0.54 μm is located in a distance z_{12} behind the sample on a motorized stage containing two additional translations. This allows for a precise alignment of the detector with respect to the optical axis. In order to minimize penumbra blurring due to the source spot, the sample is placed in close proximity to the high-resolution detector, leading to a half-period resolution well below 1 μm in 2d, as determined by an absorbing test pattern.

The experimental parameters used for imaging of a 1 mm punch from a human AD hippocampus at the laboratory setup are given in Suppl. Table S1. Note that in order to increase the field of view and visualize the entire biopsy punch, three tomographic scans were recorded at adjacent overlapping positions.

2.2.2. Synchrotron setup

The synchrotron experiments were carried out at the **G**öttingen **I**nstrument for **N**ano-**I**maging with **X**-rays (GINIX) installed at the P10 beamline of the PETRAIII storage ring at DESY in Hamburg (Salditt et al., 2015). A sketch of the main components of the setup is depicted in Fig. 1(b). The x-rays are generated by an undulator and monochromatized by a double-crystal Si(111) channel-cut monochromator to an energy of 8 keV. Further downstream, the x-rays are prefocused by a set of Kirkpatrick-Baez (KB) mirrors to an approximate focus size of 300×300 nm^2. In order to reduce high-frequency artifacts in the illumination and increase the coherence, the beam is subsequently coupled into a waveguide (Chen et al., 2015). This leads to an effective secondary source with a size below 20 nm (bidirectional). In a distance z_{01} the sample is placed on a fully motorized sample stage which allows for an alignment of the rotation axis with respect to the beam as well as a precise positioning of the region of interest within the sample in the field of view. Approximately 5 m downstream, a scintillator-based fiber-coupled sCMOS detector (Photonic Science, UK) with gadox as scintillating material and a pixel size $p = 6.5$ μm is placed in order to record the intensity images (holograms). The cone-beam geometry of the setup enables varying effective pixel sizes depending on the distance between the source and the sample (z_{01}) as well as the sample and the detector (z_{12}). Hence, by changing the magnification $M = (z_{01} + z_{12})/z_{01}$, the effective pixel size $p_{\text{eff}} = p/M$ can be tuned. The experimental parameters are listed in Suppl. Table S1. Note that two tomograms at adjacent overlapping positions were recorded in order to increase the effective field of view of the measurement.

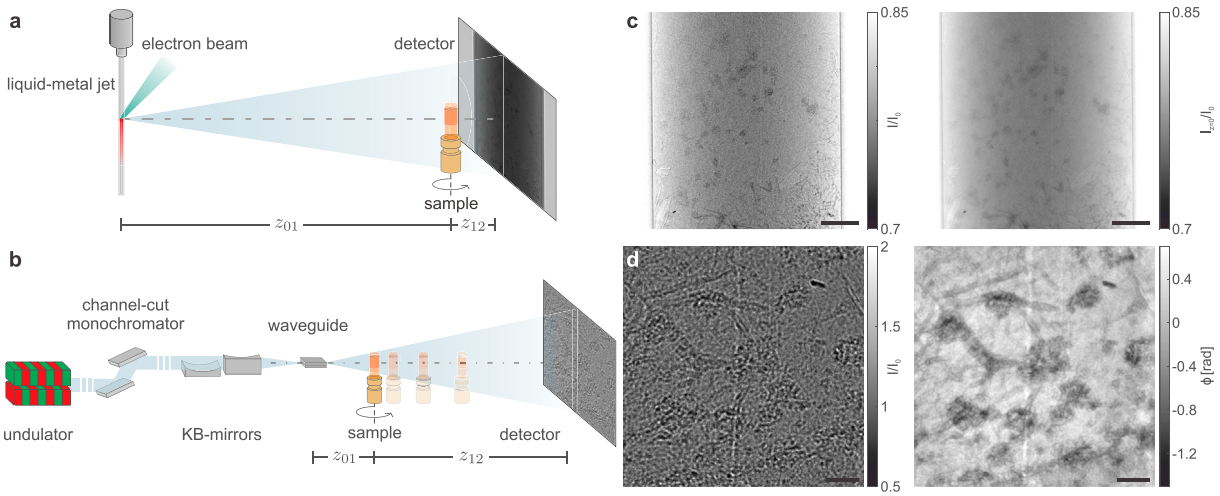

Fig. 1. Experimental realization. (a) Sketch of the laboratory setup. The x-rays are generated by a liquid-metal jet microfocus source. At a distance z_{01} behind the source, the sample is placed on a fully motorized sample tower. The intensity image is recorded by a high-resolution detector in a distance $z_{12} \ll z_{01}$ behind the sample. (b) Sketch of the synchrotron setup. The x-rays are generated by an undulator and monochromatized by a channel-cut monochromator to an energy of 8 keV. After prefocusing to ~300×300 nm^2 by a set of KB-mirrors the beam is coupled into a waveguide which further refines the beam and leads to a secondary source of below 20 nm. In a distance z_{01} behind the waveguide, the sample is placed on a fully motorized sample stage and the intensity images are recorded by an x-ray detector placed at a distance z_{12} behind the sample. (c) Exemplary empty-beam corrected projection acquired at the laboratory setup (left). The corresponding reconstructed intensity distribution in the object plane using the BAC phase retrieval approach is depicted on the right. (d) Exemplary empty-beam corrected projection acquired at the synchrotron setup (left) and corresponding reconstructed phase distribution (right) using the CTF approach with four propagation distances taken into account. Scale bars: 200 μm (c) and 50 μm (d).

3. Data analysis

3.1. Laboratory setup

Reconstruction of the intensity distribution in the object plane was carried out on the individual projections using the Bronnikov-aided correction (BAC) with the regularization parameters given in Suppl. Table S1 (see Fig. 1(c) for an exemplary projection). In order to increase the signal-to-noise ratio (SNR), all projections were resampled by a factor of 2 prior to the reconstruction step. Ring removal on the individual sinograms was performed via a wavelet-based approach (Münch et al., 2009) and tomographic reconstruction was carried out via the cone-beam implementation of the ASTRA toolbox (Palenstijn et al., 2011; van Aarle et al., 2015, 2016). To further increase the SNR, each tomographic slice was filtered with a Gaussian function with a standard deviation of 0.7 pixels. Subsequently, the three individually reconstructed volumes were manually aligned to each other and merged in Avizo Lite 9 (FEI Visualization Sciences Group, USA).

The segmentation of the different features within the reconstructed volume was also carried out in Avizo. For the mineralized plaques as well as the mineralized and unaffected blood vessels, the region growing-based *Magic Wand* tool was used which segments connected voxels starting from a manually defined seeding point which lie within a specified gray value range. In order to segment different components within the volume separately, the gray value range was adjusted with respect to the feature of interest. The cells in the granular layer were labeled manually in each slice via the threshold-based *Brush* tool which only marks pixels with a gray value within a predefined range.

3.2. Synchrotron setup

Phase retrieval of the individual projections was performed according to the contrast transfer function (CTF)-based approach for homogeneous weakly absorbing samples (Cloetens et al., 1999; Turner et al., 2004; Zabler et al., 2005; Bartels et al., 2015), assumptions which are well met by unstained biological tissue, with the regularization parameters given in Suppl. Table S1 (cf. Fig. 1(d)). In order to account for missing spatial frequencies in the acquired images caused by the zero crossings of the CTF, projections were acquired at four propagation distances. Due to the cone-beam geometry of the setup, these yield different magnifications and hence fields of view. Therefore, they were rescaled to the projection with the smallest pixel size, aligned to each other via a cross-correlation in Fourier space (Guizar-Sicairos et al., 2008) and cropped to the same field of view. Prior to tomographic reconstruction via the filtered back-projection implemented in Matlab using a standard Ram-Lak filter, a ring-removal algorithm was applied on the individual sinograms (Ketcham, 2006). Subsequently, the two individually reconstructed tomographic volumes were manually aligned and merged in Avizo. The segmentation of the reconstructed volume was carried out analogously to the laboratory data.

4. Histology

4.1. Immunohistochemistry

To correlate μCT findings with histological analysis, the 1 mm punch biopsy taken from the FFPE tissue block was re-embedded in paraffin, and serial sections were cut at 1 μm using a microtome. The tissue sections were then deparaffinized in xylene, rehydrated and transferred to 3% H_2O_2 in PBS for 20 min at 4°C to block the endogenous peroxidase. After three washing steps with PBS the sections were incubated with blocking buffer (10% fetal calf serum in PBS) for at least 20 min to reduce unspecific antibody binding. After these procedures, the sections were prepared for primary and secondary antibody incubation. Primary antibodies (anti-Phospho Tau, clone AT8, MN1020, Thermo Fisher Scientific, diluted 1:100, and anti-Amyloid beta (A4), clone 6E10, Z932002-Y, Zytomed) were diluted in blocking buffer and incubated over night at 4°C and then washed three times with PBS. Primary antibody binding was visualized by biotin-conjugated secondary antibodies, ExtrAvidin-Peroxidase and DAB. Tissue sections were incubated for 1 h with the secondary antibody diluted in blocking buffer, another 1 h with ExtrAvidin-Peroxidase 1:1000 in blocking buffer and subsequently washed with PBS. Finally DAB working solution was used to visualize the antibody binding. Thereby DAB is oxidized by the peroxidase, which produces a dark brown reaction. To confirm that the electron-dense features in the μCT results correspond to microglia accumulation in the

vicinity of the senile plaque (Suppl. Figs. S2–S5), we performed double immunohistochemistry for either KiM1P or Iba1 (anti mouse KiM1P, clone KiMP1; 1:50, kind gift of Prof. Dr. Heinz-Joachim Radzun, Göttingen, anti rabbit Iba1, 1:500, 019–19741, WAKO) on the same sections that were analyzed for Tau and Turnbull in Fig. 4. Double-labelling immunohistochemistry was performed combining DAB and Fast Blue using alkaline phosphatase-conjugated secondary antibody (Dako, 1:50). Sections were counterstained with hematoxylin, dehydrated and coverslipped with DePex mounting medium.

4.2. Turnbull staining

To detect total (ferrous and ferric) as well as ferrous non-heme iron diaminobenzidine (DAB) enhanced Turnbull staining was applied. Tissue sections were deparaffinized in xylene, rehydrated and immersed in 10% aqueous ammoniumsulfide solution in deionized water for 90 min for detection of total non-heme iron. After three washing steps with aqua dest, the sections were incubated for 15 min with aqueous solution containing 10% potassium ferricyanide and 0.5% hydrochloric acid (HCl) followed by five washing steps with PBS. Next, sections were incubated with 3% H_2O_2 in PBS for 60 min at room temperature to block endogenous peroxidase. The sections were then washed five times with PBS. Iron staining was amplified by a solution containing 0.025% DAB and 0.005% hydrogen peroxide in PBS for 20 min and stopped by rinsing the sections in tap water. Sections were counterstained with hematoxylin, dehydrated and coverslipped with DePex mounting medium.

4.3. Microscopy

Microscopic images were created with an Olympus BX60 Upright Compound Microscope using a 10× objective. Several images were acquired at adjacent positions in order to image the entire histological section and subsequently stitched together in Fiji using the Grid/Collection stitching plugin (Preibisch et al., 2009).

5. Results

5.1. Virtual 3d histology by phase-contrast tomography

Virtual slices through the reconstructed volumes of hippocampal human brain tissue affected by Alzheimer's disease obtained at a laboratory setup and at the holo-tomography endstation GINIX are shown in Fig. 2. Within the slices, the granular layer of the dentate gyrus is well visible due to the high cell density as well as the neighboring molecular and polymorphic layer. In addition, structures with a significantly higher electron density compared to the surrounding tissue can be observed. On the one hand, these structures, which are exclusively found in the molecular layer of the dentate gyrus, can be identified as mineralized blood vessels due to the accumulation of electron-dense deposits in the vascular wall. These structurally altered blood vessels are not a typical hallmark of Alzheimer's disease but may occur independently, as has been shown previously in the context of hippocampal vascular fibrosis and calcification (Wegiel et al., 2002). On the other hand, plaque-like features can be identified in close proximity to these mineralized blood vessels whose spatial distribution follows the shape of the granular layer.

To better visualize the structural organization of these specific features in three dimensions, a semi-automatic gray value-based segmentation was carried out for both the data obtained at the laboratory and the GINIX setup. The results are shown in Fig. 3 as well as in Suppl. Movie S1. In the laboratory-based segmentation, the cell-rich band of the granular

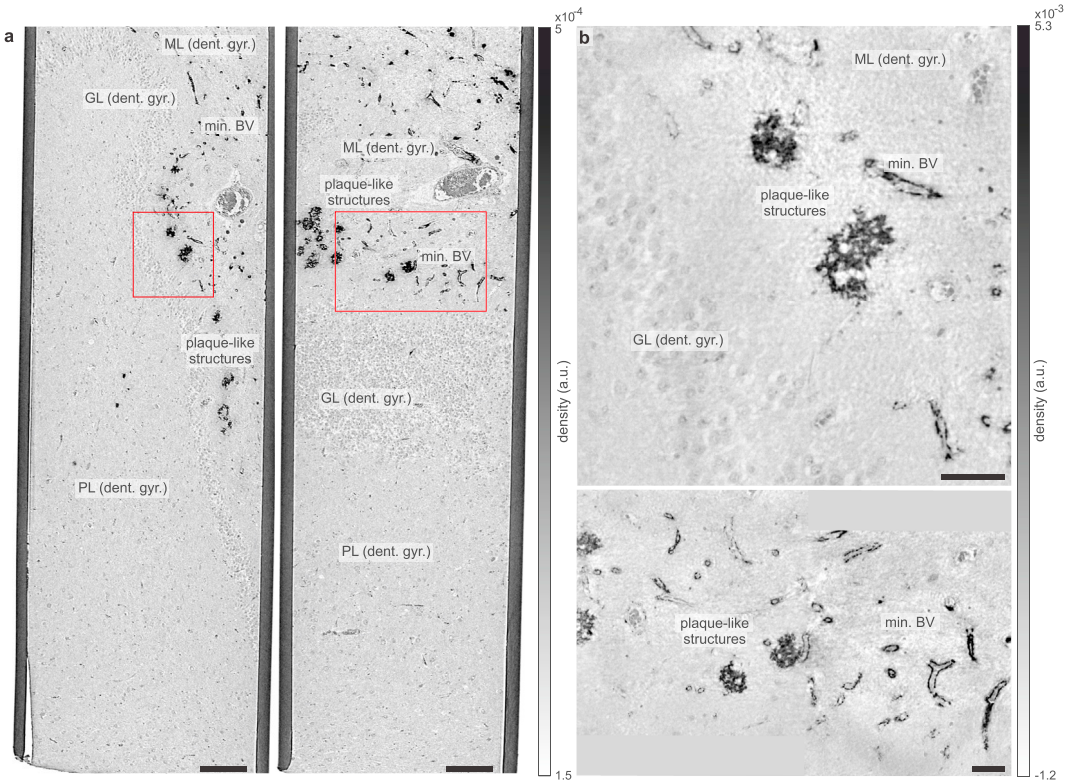

Fig. 2. Virtual slices through the reconstructed volumes of a 1 mm punch from a human AD hippocampus. (a) Two orthogonal slices obtained at the laboratory setup. The effective field of view was enlarged by acquiring and merging three tomograms at adjacent positions in height. Features as the granular (GL), molecular (ML) and polymorphic layer (PL) of the dentate gyrus, as well as mineralized blood vessels and electron-dense plaque-like structures can be recognized. (b) Corresponding virtual slices through the dataset obtained at the synchrotron. As in the laboratory measurements, the field of view was artificially increased by merging two adjacent tomograms. The position of the measurements with respect to the entire punch is indicated by the rectangles in (a). Compared to the laboratory measurements the cells in the granular layer as well as the mineralized blood vessels and plaque-like structures can be resolved at higher detail. Scale bars: 200 μm (a) and 50 μm (b).

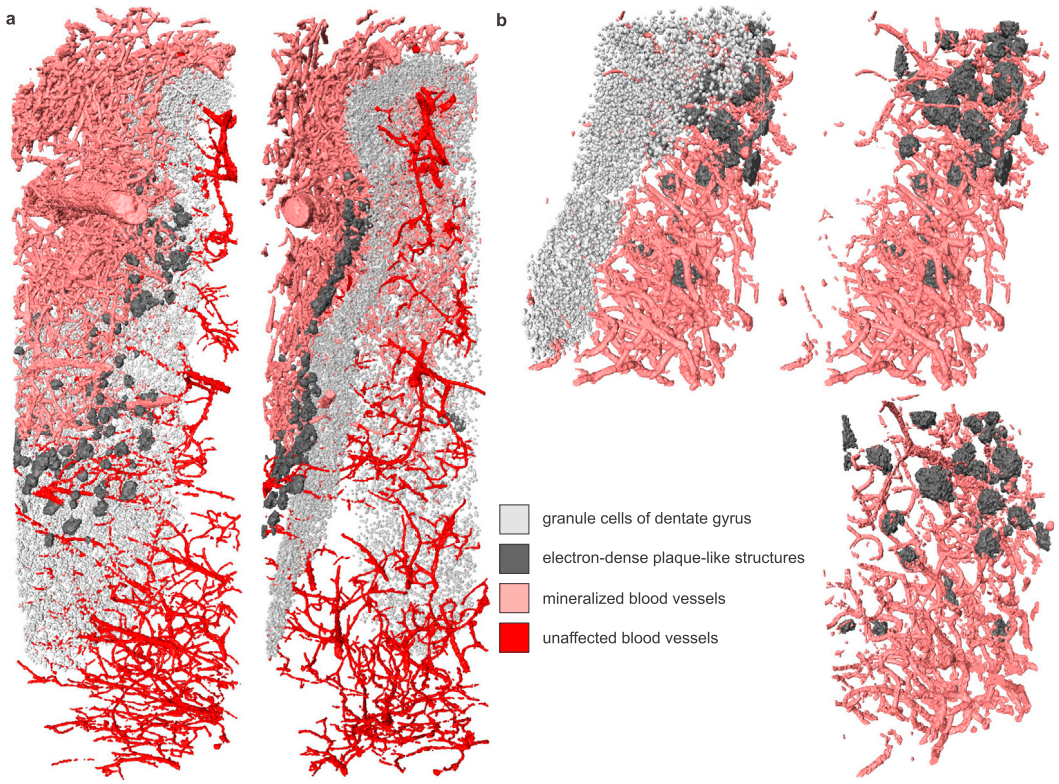

Fig. 3. 3d visualization of the acquired datasets. (a) Segmentation of the reconstructed volume of the entire 1 mm punch obtained at the laboratory setup. Cells of the granular layer are depicted in light gray, unaffected blood vessels in red, mineralized blood vessels in light red and the electron-dense plaque-like structures in dark gray. The spatial distribution of the different features shows that the electron-dense plaque-like structures are located in close proximity to both the granular layer as well as the mineralized blood vessels and that both types of vessels are separated by the cellular band of the granular layer. (b) Segmentation of the dataset obtained at the synchrotron. The segmentation is depicted both with the cells of the granular layer and without in order to emphasize the close proximity of the electron-dense plaque-like structures to the mineralized blood vessels.

layer is depicted in light gray, enclosing the polymorphic layer on the right while the molecular layer is located on the left, unaffected blood vessels are rendered in red and mineralized blood vessels in light red. It is evident that within the polymorphic layer only non-mineralized blood vessels can be found whereas in the molecular layer the majority of blood vessels exhibits electron-dense deposits in the vascular wall. The electron-dense plaque-like features, depicted in dark gray, are exclusively found in the molecular layer in close proximity to the granular layer, following its general shape. The same behavior can be recognized in the segmentation results of the synchrotron data, shown in Fig. 3(b), in which the spatial relation between the plaque-like features, the mineralized blood vessels and the cells of the granular layer can be observed at higher detail.

Supplementary data related to this article can be found at https://doi.org/10.1016/j.neuroimage.2020.116523.

5.2. Correlation with histology in regions with senile plaques

As contrast formation in x-ray tomography relies on differences in electron-density, the exact nature of the observed features cannot be unambiguously resolved as more specific information such as elemental composition is not encoded within the results. Hence, we combined the tomographic experiments with histology. To this end, the scanned sample was re-embedded in paraffin and histological sections of 1 µm thickness were created. Fig. 4 shows consecutive sections stained according to the Turnbull protocol (center), which visualizes iron, or via a Tau antibody stain (right), which is used to identify neurofibrillary tangles, neuropil threads and abnormal neurites in senile plaques.

Additionally, a counterstain by hematoxylin was used to visualize cells and calcified material. The corresponding virtual slice through the µCT result obtained at the laboratory setup is shown on the left.

In order to correlate these results, a manual alignment was performed in which specific hallmarks as the shape of the granular layer or the highly contrasted mineralized blood vessels were identified within the 3d volume. Based on these findings, a virtual slice was placed through the 3d object which included these features. The entire procedure was carried out in Avizo Lite 9. As only planar slices can be considered in the *Slice* module used for creating virtual sections in any arbitrary direction, a curved surface could not be realized, as is necessary in order to account for small sample deformations which might occur during the re-embedding or slicing of the specimen. Hence, small morphological changes between the virtual slice and the actual histological section exist. However, as indicated by the encircled features in the virtual µCT results on the left and the histological sections stained according to the Turnbull protocol in the center, a large number of similarities were found between these two imaging modalities. This justifies the assumption that the position of both slices coincides and that a valid comparison can be made.

The results show that the electron-dense deposits around the vascular wall of the blood vessels in the molecular layer mainly contain iron and calcified material, as both the Turnbull protocol and the hematoxylin show positive results for these structures. Additionally, two senile plaques can be observed due to the Tau antibody stain shown on the right in the vicinity of the granular layer of the dentate gyrus (arrows). However, the comparison with the µCT results reveals that these plaques can actually not directly be seen by means of x-ray phase-contrast tomography, showing that the electron density differences to the surrounding tissue are too insignificant to create enough contrast. The most striking structural alteration which occurs in the vicinity of the plaque is a gap in the cellular band of the granular layer which can also be observed in the histological sections, again proving the consistency between the two

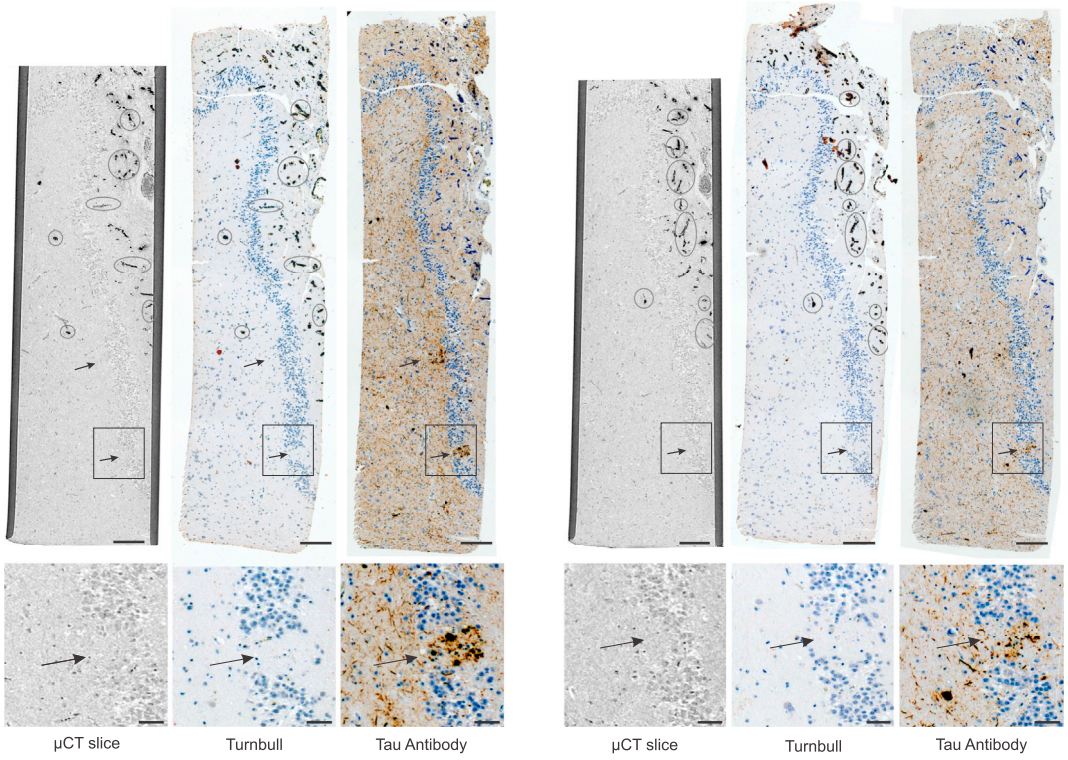

Fig. 4. Comparison between virtual slices through the laboratory μCT results (left) and histological sections in a region showing 'native' β-amyloid plaques. In the histological sections, iron was stained according to the Turnbull protocol (center) and neurofibrillary tangles, neuropil threads and abnormal neurites in senile plaques were identified via a Tau antibody stain. A counterstain by hematoxylin was used to visualize cells and the tissue structure. The encircled features indicate similarities between the μCT and histology results, showing that the visually determined virtual slice through the μCT dataset corresponds relatively well to the actual slice from the histological sectioning. The comparison demonstrates that features like the mineralized blood vessels, especially the iron rich clusters around the vessels, or the cells of the granular layer of the dentate gyrus can be very well imaged by the μCT experiments, indicating that these exhibit a significantly higher electron density compared to the surrounding tissue. Features as the senile plaques (arrows), however, can only be identified due to the missing cells in the band of the granular layer and therefore exhibit no significant difference in electron density. Note that the contrast in the microscope images of the histology sections has been adjusted to ensure maximum visibility of the features of interest. Scale bars: 200 μm (top) and 50 μm (bottom).

imaging modalities. As this gap is a good indicator for the position of the plaque in the μCT results, a more detailed visualization of the micro-environment of the senile plaques can be made, as depicted in Suppl. Figs. S2 and S3. Here, a larger number of virtual slices covers the entire plaque-region, showing that slight changes of the tissue structure itself, which might be associated with the β-amyloid protein, as well as an accumulation of microglia, appearing as small dark spots within the plaque region, can be observed. This accumulation of microglia might serve as an indirect marker for senile plaques in unstained human tissue, but would also be of interest by itself due to their role in senile plaque formation (Mackenzie et al., 1995; Simard et al., 2006). It can also be visualized by maximum intensity projections over 60 consecutive slices (Suppl. Figs. S4 and S5), in which the accumulation of microglia in the plaque area can be well recognized whereas the plaque itself remains invisible as it does not have a larger electron density compared to the surrounding tissue.

The assumption that the small cells are indeed microglia is justified when considering the histological sections in Suppl. Fig. S6, which are the same sections as in Fig. 4 with additional staining for microglia and macrophages. While microglia exist throughout the tissue, a clear accumulation of these cells can be observed within the plaque region. Since other cells such as the dentate granule cells are missing in this region, the small cells found in the μCT reconstructions can be identified as these microglia or rather their electron-dense nuclei. This can be further validated by a one-to-one comparison between the two imaging modalities, as shown in Suppl. Fig. S7. Note that the μCT slices are not exactly the same as in Fig. 4 as in this case the alignment was focused on the microglia and not the mineralized blood vessels. Due to morphological changes during re-embedding of the sample it is impossible to take all features of interest into account as long as only planar virtual slices through the reconstructed density distribution are considered. The comparison confirms the assumption that the small electron-dense features in the μCT results correspond to microglia which accumulate in the vicinity of the senile plaque.

5.3. *Correlation with histology in regions with electron-dense plaque-like features*

As 'native' senile plaques are not directly visible in the μCT results, the question arises as to the nature of the electron dense plaque-like structures. To clarify this, histological sections were created within the corresponding region of the punch, as shown in Fig. 5.

Iron was again visualized according to the Turnbull staining protocol (center) whereas neurofibrillary tangles, neuropil threads and dystrophic neurites surrounding senile plaques were identified via a Tau antibody stain in a consecutive slice (right). As in the previous case, similar features which can be found both in the μCT reconstructions and the histological sections were used for manual alignment of the results of the two imaging modalities. The high structural correlation between the two again proves the validity of a comparison. The results obtained via the Turnbull staining protocol show that the observed plaque-like features contain iron which explains their high contrast in the μCT results. Furthermore, the hematoxylin staining results in blue colour, indicating that they also contain calcified material. The Tau antibody stain, however, does not show a positive reaction which suggests that these plaque-like structures are indeed not senile plaques.

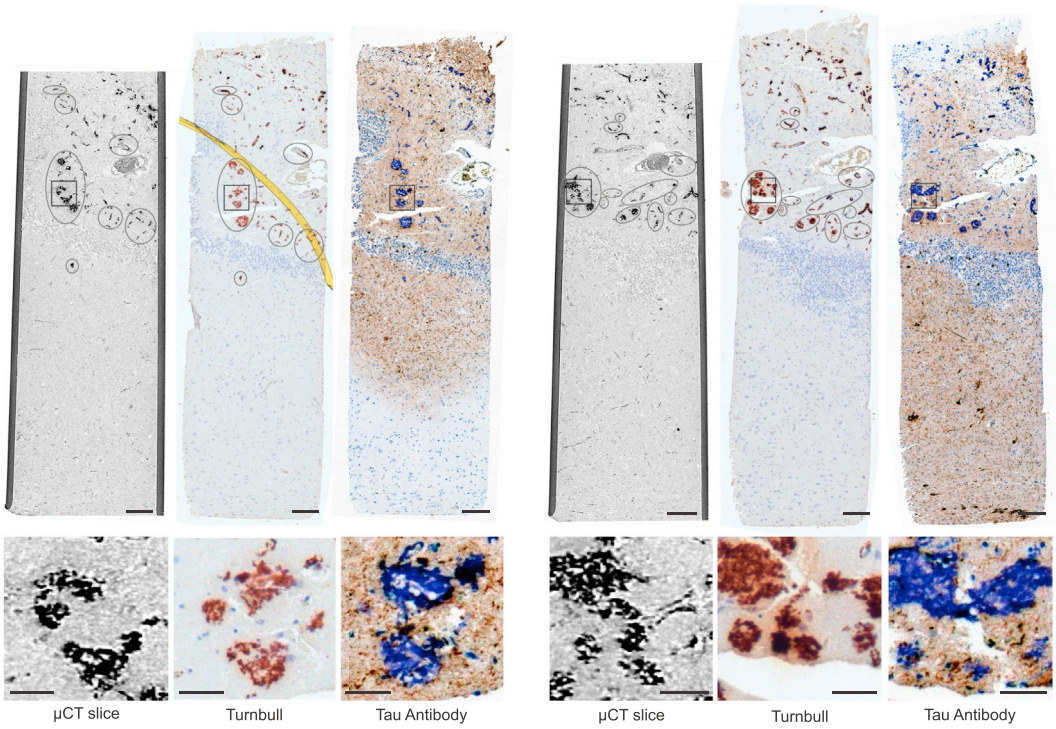

Fig. 5. Comparison between virtual slices through the laboratory μCT results (left) and histological sections in a region showing electron-dense plaque-like structures. As in the case of the slices shown in Fig. 4, iron was visualized according to the Turnbull staining protocol (center) whereas neurofibrillary tangles, neuropil threads and abnormal neurites in senile plaques were identified via a Tau antibody stain in a neighboring slice (right). Similar features in the virtual slice and the histological sections, marked by ellipses, indicate approximately coincident positions. A comparison between the results shows that the observed plaque-like structures, which have a high electron density according to the μCT results, correspond to features containing iron as well as calcified material as they are both positive in the Turnbull stain as well as in the hematoxylin stain on the right. The Tau antibody, however, does not show a positive reaction within these structures. Note that the contrast in the microscope images of the histology sections has been adjusted to ensure maximum visibility of the features of interest. Scale bars: 200 μm (top) and 50 μm (bottom).

As the Tau antibody stain, however, only visualizes dystrophic neurites in senile plaques and not the β-amyloid, we additionally stained for the protein itself to clarify whether the electron-dense structures could be associated with a mineralized form of β-amyloid plaques. The results are depicted in Fig. 6, in which encircled features in both the μCT result and the section stained according to the Turnbull protocol again indicate similarities between the two. Also in this example, the electron-dense structures show iron, as can be especially well recognized in the magnified regions at the bottom. The β-amyloid stain reveals that they consist of a mixture of calcified structures and β-amyloid since both blue and brown colored components can be recognized within the region of interest. This proves that the electron-dense plaque-like structures are indeed mineralized β-amyloid plaques which have a significantly higher electron density than their unaffected counterparts due to the accumulation of iron and calcium and presumably other elements which have not been stained in this study.

6. Discussion

In the present work we have combined 3d virtual histology by means of propagation-based phase-contrast tomography and classical histology on hippocampal human brain tissue affected by Alzheimer's disease. We have used two different custom-built setups, enabling visualization of the cytoarchitecture on the cellular and sub-cellular level. While the laboratory instrument offers larger fields of view, and already a surprisingly good feature observability in tissue, fine details for example of the mineralized plaques and blood vessels are revealed by the synchrotron setup at increased magnification and resolution. Note that following the development of liquid jet anode sources, laboratory CT has reached cellular resolution in unstained soft tissue (Vågberg et al., 2015). However, the reconstructions with synchrotron radiation offer not only higher resolution but also more quantitative contrast values. For this reason, the synchrotron results can be used as ground truth to 'calibrate' the data analysis workflow of the laboratory results, in particular in view of segmentation. The difference in image quality and feature observability can be appreciated best in Fig. 2, showing that the gap between the two modalities is smaller than commonly expected. In particular, we can already identify the main anatomical features of the hippocampus, such as the cells of the dentate granular layer or its vessel architecture, based on the advanced laboratory μCT setup and reconstruction workflow, which we have both optimized for unstained paraffin-embedded tissue. This makes this imaging method a promising tool for the visualization of structural alterations in the course of Alzheimer's disease. The accessibility and high availability of laboratory instrumentation without the need to apply for beamtime allows for the analysis of a comparably large number of autopsy brain tissue from individuals with different degree of AD progression. The fact that the same sample can subsequently be examined via histology opens up the unique possibility of correlating information, with the added benefit that the entire 3d volume can be interrogated. For this purpose, a few representations of a characteristic morphological structure are investigated in one histological section, for example in view of a specific protein, and the entire set of similar features can be evaluated in the entire 3d reconstruction volume for statistical evaluation. At the same time, volume-penetrating labelling and staining methods should be developed, which are specific for relevant proteins and offer high x-ray phase contrast. The contrast of typical hallmarks of Alzheimer's disease could be enhanced, for example, by radiocontrast agents coupled to antibodies. Radiocontrast agents are electron-dense

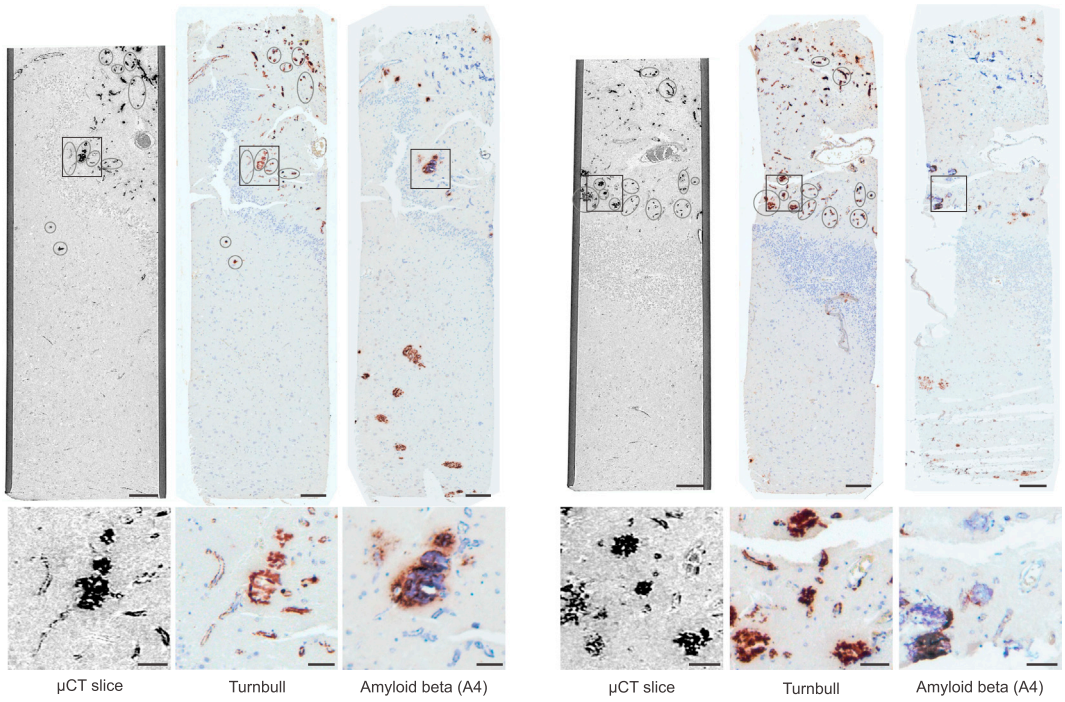

Fig. 6. Comparison between virtual slices through the laboratory µCT results (left) and histological sections using a β-amyloid (A4) staining protocol (right). As in Figs. 4 and 5, the encircled features in the virtual slice and the histological sections show similarities which indicate that the positions of the virtual slices from the µCT results and the histological sections approximately coincide. Also in this case, the electron-dense plaque-like structures correspond to features containing iron, as observed in the corresponding histological section stained according to the Turnbull protocol (center). The β-amyloid (A4) together with the hematoxylin stain additionally shows that they consist of calcified structures and β-amyloid, proving that they are indeed mineralized β-amyloid plaques. Note that the contrast in the microscope images of the histology sections has been adjusted to ensure maximum visibility of the features of interest. Scale bars: 200 µm (top) and 50 µm (bottom).

materials with a high atomic number, e.g., osmium tetroxide, as shown in (Dyer et al., 2017; Massimi et al., 2019) for mouse brain tissue, or silver which is used in the Bielschowsky technique, a standard staining procedure in histology. In order to establish more advanced protocols, correlative x-ray tomography and histology as used here will be indispensable. But also for unstained tissue volumes we anticipate that a wide range of morphological metrics could be established to quantify and classify AD tissue phenotypes. For example, neuron density, shape parameters, and neighborhood relations could be derived directly based on the electron density distribution. However, in order to exploit this information in a meaningful way for AD research, in a first step many samples have to be scanned in combination with automated feature extraction and possibly also machine learning.

Notwithstanding the necessity of screening many samples in order to draw conclusion on morphological alterations based on 3d reconstructions, a wealth of information is already provided by an in depth study of an individual affected by the disease, as demonstrated here. The patient considered in this work showed the typical anatomical hallmarks of Alzheimer's disease, namely β-amyloid plaques and neurofibrillary tangles, but in addition also mineralized blood vessels as well as mineralized plaques in the molecular layer of the dentate gyrus. These mineralized plaques were observed in close vicinity to the mineralized vessels. The strong contrast of these features facilitated the unambiguous identification of the same regions within the µCT reconstruction volume and the histological sections. It also helped to distinguish different kinds of plaques and to delineate the visibility of different structural hallmarks with phase-contrast tomography. Not surprisingly, the analysis revealed that mineralized plaques, containing iron as well as calcified material, have a high electron density compared to surrounding tissue and hence a good contrast in the µCT results whereas unmineralized senile plaques exhibit rather small contrast. The fact that the mineralized plaques also show a positive reaction in the β-amyloid stain whereas the Tau antibody does not lead to an immunohistochemical response indicates that they either do not contain dystrophic neurites or that the mineralization leads to a loss of immunoreactivity to the Tau antibody. The latter hypothesis is supported by the observation that in other regions of the hippocampus where both mineralized and unaffected plaques occur (see overview histological section in Suppl. Fig. S1), Tau positive features and calcified material can be identified in parallel within the plaque region. Furthermore, previous studies on vessel calcifications in the hippocampus have reported a partial or total loss of immunoreactivity with antibodies to β-amyloid for plaques found in the molecular layer of the dentate gyrus (Wegiel et al., 2002).

Although the senile plaques are not directly visible in the µCT results, indirect markers for the occurrence of these plaques can be observed as, e.g., neuronal cell loss in the region occupied by the plaque as well as an accumulation of microglia (cf. Suppl. Figs. S2–S7). Hence, in subsequent studies of Alzheimer's disease it might be possible to identify plaque locations based on these structural alterations and to study their microenvironment in terms of cellular and vascular distributions in three dimensions via x-ray phase-contrast tomography. Recruitment of microglia to AD plaques would be a very interesting phenomenon to be investigated by µCT. The fact that beta-amyloid plaques in human tissue are not immediately visible in the tomographic reconstructions is in contradiction to previous studies using mouse models of Alzheimer's disease, see (Noda-Saita et al., 2006; Connor et al., 2009; Pinzer et al., 2012; Astolfo et al., 2016; Massimi et al., 2019). This body of literature comprises both crystal- (Noda-Saita et al., 2006; Connor et al., 2009) and grating-based phase contrast (Pinzer et al., 2012), as well as propagation imaging (Astolfo et al., 2016; Massimi et al., 2019). Despite the much lower resolution in (Noda-Saita et al., 2006; Connor et al., 2009; Pinzer et al., 2012; Astolfo et al., 2016), bright spots in the tissue of mouse mutants were observed, which could be attributed to amyloid deposits. These results were obtained for fixated, unstained and hydrated preparations.

One may be tempted to suspect that the presence and absence of visible plaques in the x-ray reconstructions depends on sample preparation. However, if the electron density contrast of plaques was sufficiently high to stand out against hydrated tissue, this would also be likely to be the case for paraffin-embedded samples. Further, β-amyloid plaques were also very well resolved in nano-CT of dehydrated, heavy-metal stained preparations of mouse mutants (Massimi et al., 2019). Neither do we have reason to believe that paraffin embedding destroys the amyloid structures. Therefore, differences with respect to preparation or imaging modality seem unlikely as an explanation for the discrepancy of the present study with x-ray tomography literature. Instead, it seems plausible to attribute this to structural differences between the β-amyloid plaques in human tissue and those in mouse models. After all, it is well known that AD mouse models are geared towards an extremely early and fast development of AD symptoms based on excessively high expression levels of Amyloid precursor protein (APP) or the PSEN1 subunit of the γ-secretase, see the critical discussion in (King, 2018). As a result, the deposits in mouse mutants could be much larger and possibly also of higher electron density than in humans. This result underlines the necessity to study AD pathologies directly in human brain tissue.

Acknowledgements

We thank Michael Sprung for support at the P10 beamline as well as Katja Schulz, Heidi Brodmerkel and Jasmin Reichl for histological technical support. We are also grateful for generous beamtime allocation. This work was supported by the Deutsche Forschungsgemeinschaft (DFG, German Research Foundation) under Germany's Excellence Strategy - EXC 2067/1–390729940.

Appendix A. Supplementary data

Supplementary data to this article can be found online at https://doi.org/10.1016/j.neuroimage.2020.116523.

References

Astolfo, A., Lathuiliere, A., Laversenne, V., Schneider, B., Stampanoni, M., 2016. Amyloid-β plaque deposition measured using propagation-based X-ray phase contrast CT imaging. J. Synchrotron Radiat. 23 (3), 813–819.

Bartels, M., Hernandez, V.H., Krenkel, M., Moser, T., Salditt, T., 2013. Phase contrast tomography of the mouse cochlea at microfocus x-ray sources. Appl. Phys. Lett. 103 (8), 083703.

Bartels, M., Krenkel, M., Cloetens, P., Möbius, W., Salditt, T., 2015. Myelinated mouse nerves studied by x-ray phase contrast zoom tomography. J. Struct. Biol. 192 (3), 561–568.

Bech, M., Bunk, O., Donath, T., Feidenhans, R., David, C., Pfeiffer, F., 2010. Quantitative x-ray dark-field computed tomography. Phys. Med. Biol. 55 (18), 5529.

Chapman, D., Thomlinson, W., Johnston, R.E., Washburn, D., Pisano, E., Gmür, N., Zhong, Z., Menk, R., Arfelli, F., Sayers, D., 1997. Diffraction enhanced x-ray imaging. Phys. Med. Biol. 42 (11), 2015.

Chen, H.-Y., Hoffmann, S., Salditt, T., 2015. X-ray beam compression by tapered waveguides. Appl. Phys. Lett. 106 (19), 194105.

Cloetens, P., Ludwig, W., Baruchel, J., Van Dyck, D., Van Landuyt, J., Guigay, J.P., Schlenker, M.a., 1999. Holotomography: quantitative phase tomography with micrometer resolution using hard synchrotron radiation x rays. Appl. Phys. Lett. 75 (19), 2912–2914.

Connor, D.M., Benveniste, H., Dilmanian, F.A., Kritzer, M.F., Miller, L.M., Zhong, Z., 2009. Computed tomography of amyloid plaques in a mouse model of Alzheimer's disease using diffraction enhanced imaging. Neuroimage 46 (4), 908–914.

Deng, J., Lo, Y.H., Gallagher-Jones, M., Chen, S., Pryor, A., Jin, Q., Hong, Y.P., Nashed, Y.S., Vogt, S., Miao, J., Jacobsen, C., 2018. Correlative 3d x-ray fluorescence and ptychographic tomography of frozen-hydrated green algae. Sci. Adv. 4 (11) eaau4548.

Dyer, E.L., Roncal, W.G., Prasad, J.A., Fernandes, H.L., Gürsoy, D., De Andrade, V., Fezzaa, K., Xiao, X., Vogelstein, J.T., Jacobsen, C., et al., 2017. Quantifying mesoscale neuroanatomy using X-ray microtomography. eNeuro 4 (5). ENEURO–0195.

Elder, G.A., Gama Sosa, M.A., De Gasperi, R., 2010. Transgenic mouse models of Alzheimer's disease. MSJM (Mt. Sinai J. Med.): A Journal of Translational and Personalized Medicine: A Journal of Translational and Personalized Medicine 77 (1), 69–81.

Guizar-Sicairos, M., Thurman, S.T., Fienup, J.R., 2008. Efficient subpixel image registration algorithms. Opt. Lett. 33 (2), 156–158.

Hemberg, O., Otendal, M., Hertz, H., 2003. Liquid-metal-jet anode electron-impact x-ray source. Appl. Phys. Lett. 83 (7), 1483–1485.

Hieber, S.E., Bikis, C., Khimchenko, A., Schweighauser, G., Hench, J., Chicherova, N., Schulz, G., Müller, B., 2016. Tomographic brain imaging with nucleolar detail and automatic cell counting. Sci. Rep. 6, 32156.

Holme, M.N., Schulz, G., Deyhle, H., Weitkamp, T., Beckmann, F., Lobrinus, J.A., Rikhtegar, F., Kurtcuoglu, V., Zanette, I., Saxer, T., Müller, B., 2014. Complementary X-ray tomography techniques for histology-validated 3D imaging of soft and hard tissues using plaque-containing blood vessels as examples. Nat. Protoc. 9 (6), 1401.

Hyman, B.T., Phelps, C.H., Beach, T.G., Bigio, E.H., Cairns, N.J., Carrillo, M.C., Dickson, D.W., Duyckaerts, C., Frosch, M.P., Masliah, E., Mirra, S.S., Nelson, P.T., Schneider, J.A., Thal, D.R., Thies, B., Trojanowski, J.Q., Vinters, H.V., Montine, T.J., 2012. National Institute on Aging–Alzheimer's Association guidelines for the neuropathologic assessment of Alzheimer's disease. Alzheimer's Dementia 8 (1), 1–13.

Ketcham, R.A., 2006. New algorithms for ring artifact removal. Proc. SPIE 6318, 63180O–63180O–7.

Khimchenko, A., Bikis, C., Pacureanu, A., Hieber, S.E., Thalmann, P., Deyhle, H., Schweighauser, G., Hench, J., Frank, S., Müller-Gerbl, M., et al., 2018. Hard X-ray nanoholotomography: large-scale, label-free, 3D neuroimaging beyond optical limit. Advanced Science 1700694.

King, A., 2018. A model challenge: developing better models of Alzheimer's disease could be key to stemming the continued clinical failure of treatments. Nature 559, S13–S15.

Li, A., Gong, H., Zhang, B., Wang, Q., Yan, C., Wu, J., Liu, Q., Zeng, S., Luo, Q., 2010. Micro-optical sectioning tomography to obtain a high-resolution atlas of the mouse brain. Science 330 (6009), 1404–1408.

Mackenzie, I.R., Hao, C., Munoz, D.G., 1995. Role of microglia in senile plaque formation. Neurobiol. Aging 16 (5), 797–804.

Massimi, L., Bukreeva, I., Santamaria, G., Fratini, M., Corbelli, A., Brun, F., Fumagalli, S., Maugeri, L., Pacureanu, A., Cloetens, P., et al., 2019. Exploring Alzheimer's disease mouse brain through X-ray phase contrast tomography: from the cell to the organ. Neuroimage 184, 490–495.

Momose, A., Takeda, T., Itai, Y., Hirano, K., 1996. Phase-contrast X-ray computed tomography for observing biological soft tissues. Nat. Med. 2 (4), 473–475.

Mu, Y., Gage, F.H., 2011. Adult hippocampal neurogenesis and its role in Alzheimer's disease. Mol. Neurodegener. 6 (1), 85.

Münch, B., Trtik, P., Marone, F., Stampanoni, M., 2009. Stripe and ring artifact removal with combined wavelet-Fourier filtering. Opt. Express 17 (10), 8567–8591.

Noda-Saita, K., Yoneyama, A., Shitaka, Y., Hirai, Y., Terai, K., Wu, J., Takeda, T., Hyodo, K., Osakabe, N., Yamaguchi, T., et al., 2006. Quantitative analysis of amyloid plaques in a mouse model of Alzheimer's disease by phase-contrast X-ray computed tomography. Neuroscience 138 (4), 1205–1213.

Ourselin, S., Roche, A., Subsol, G., Pennec, X., Ayache, N., 2001. Reconstructing a 3D structure from serial histological sections. Image Vis Comput. 19 (1–2), 25–31.

Paganin, D., Nugent, K.A., 1998. Noninterferometric phase imaging with partially coherent light. Phys. Rev. Lett. 80, 2586–2589.

Palenstijn, W., Batenburg, K., Sijbers, J., 2011. Performance improvements for iterative electron tomography reconstruction using graphics processing units (GPUs). J. Struct. Biol. 176 (2), 250–253.

Perl, D.P., 2010. Neuropathology of alzheimer's disease, mount sinai. J. Med.: A Journal of Translational and Personalized Medicine: A Journal of Translational and Personalized Medicine 77 (1), 32–42.

Pfeiffer, F., Bech, M., Bunk, O., Kraft, P., Eikenberry, E.F., Brönnimann, C., Grünzweig, C., David, C., 2008. Hard-x-ray dark-field imaging using a grating interferometer. Nat. Mater. 7, 134–137.

Pinzer, B., Cacquevel, M., Modregger, P., McDonald, S., Bensadoun, J., Thuering, T., Aebischer, P., Stampanoni, M., 2012. Imaging brain amyloid deposition using grating-based differential phase contrast tomography. Neuroimage 61 (4), 1336–1346.

Preibisch, S., Saalfeld, S., Tomancak, P., 2009. Globally optimal stitching of tiled 3D microscopic image acquisitions. Bioinformatics 25 (11), 1463–1465.

Salditt, T., Osterhoff, M., Krenkel, M., Wilke, R.N., Priebe, M., Bartels, M., Kalbfleisch, S., Sprung, M., 2015. Compound focusing mirror and X-ray waveguide optics for coherent imaging and nano-diffraction. J. Synchrotron Radiat. 22 (4), 867–878.

Simard, A.R., Soulet, D., Gowing, G., Julien, J.-P., Rivest, S., 2006. Bone marrow-derived microglia play a critical role in restricting senile plaque formation in alzheimer's disease. Neuron 49 (4), 489–502.

Töpperwien, M., Krenkel, M., Vincenz, D., Stöber, F., Oelschlegel, A.M., Goldschmidt, J., Salditt, T., 2017. Three-dimensional mouse brain cytoarchitecture revealed by laboratory-based x-ray phase-contrast tomography. Sci. Rep. 7, 42847.

Töpperwien, M., Van der Meer, F., Stadelmann, C., Salditt, T., 2018. Three-dimensional virtual histology of human cerebellum by X-ray phase-contrast tomography. Proc. Natl. Acad. Sci. 115 (27), 6940–6945.

Turner, L., Dhal, B., Hayes, J., Mancuso, A., Nugent, K., Paterson, D., Scholten, R., Tran, C., Peele, A., 2004. X-ray phase imaging: demonstration of extended conditions for homogeneous objects. Opt. Express 12 (13), 2960–2965.

Vågberg, W., Larsson, D.H., Li, M., Arner, A., Hertz, H.M., 2015. X-ray phase-contrast tomography for high-spatial-resolution zebrafish muscle imaging. Sci. Rep. 5 https://doi.org/10.1038/srep16625, 16625 EP –, article. URL.

Vågberg, W., Persson, J., Szekely, L., Hertz, H.M., 2018. Cellular-resolution 3D virtual histology of human coronary arteries using x-ray phase tomography. Sci. Rep. 8 (1), 11014.

van Aarle, W., Palenstijn, W.J., De Beenhouwer, J., Altantzis, T., Bals, S., Batenburg, K.J., Sijbers, J., 2015. The ASTRA Toolbox: a platform for advanced algorithm development in electron tomography. Ultramicroscopy 157, 35–47.

van Aarle, W., Palenstijn, W.J., Cant, J., Janssens, E., Bleichrodt, F., Dabravolski, A., De Beenhouwer, J., Batenburg, K.J., Sijbers, J., 2016. Fast and flexible X-ray tomography using the ASTRA toolbox. Opt. Express 24 (22), 25129–25147.

Wegiel, J., Kuchna, I., Wisniewski, T., de Leon, M., Reisberg, B., Pirttila, T., Kivimaki, T., Lehtimaki, T., 2002. Vascular fibrosis and calcification in the hippocampus in aging, Alzheimer disease, and Down syndrome. Acta Neuropathol. 103 (4), 333–343.
Zabler, S., Cloetens, P., Guigay, J.-P., Baruchel, J., Schlenker, M., 2005. Optimization of phase contrast imaging using hard x rays. Rev. Sci. Instrum. 76 (7), 073705.
Zanette, I., Zhou, T., Burvall, A., Lundström, U., Larsson, D.H., Zdora, M., Thibault, P., Pfeiffer, F., Hertz, H.M., 2014. Speckle-based X-ray phase-contrast and dark-field imaging with a laboratory source. Phys. Rev. Lett. 112 (25), 253903.